Caloris Basin: An Enhanced Source for Potassium in Mercury's Atmosphere

ANN L. SPRAGUE,* RICHARD W. H. KOZLOWSKI,
DONALD M. HUNTEN

Enhanced abundances of neutral potassium (K) in the atmosphere of Mercury have been found above the longitude range containing Caloris Basin. Results of a large data set including six elongations of the planet between June 1986 and January 1988 show typical K column abundances of ~5.4 × 10^8 K atoms/cm^2. During the observing period in October 1987, when Caloris Basin was in view, the typical K column was ~2.7 × 10^9 K atoms/cm^2. Another large value (2.1 × 10^9 K atoms/cm^2) was seen over the Caloris antipode in January 1988. This enhancement is consistent with an increased source of K from the well-fractured crust and regolith associated with this large impact basin. The phenomenon is localized because at most solar angles, thermal alkali atoms cannot move more than a few hundred kilometers from their source before being lost to ionization by solar ultraviolet radiation.

NEUTRAL SODIUM (NA) AND POTASSIUM (K) have been frequently observed in the atmosphere (*1*) of Mercury since their discovery by Potter and Morgan (*2, 3*). Much uncertainty and discussion has been associated with the source and distribution of these constituents. McGrath *et al.* (*4*) have attributed the source to photon or charged particle sputtering and subsequent evaporation from the surface regolith. Morgan *et al.* (*5*) proposed a source composed of a mixture of volatilized micrometeoritic and surface material. Sprague (*6*) has fitted observed Na and K abundances at both Mercury and the Moon with a model of atoms diffusing (*7*) from rocks at depth along grain boundaries and micro-cracks. Potter and Morgan (*8*) presented evidence that a major influence on the distribution of Na about the planet was pressure due to radiation acceleration, while Tyler *et al.* (*9, 10*) reported latitudinal asymmetries in both K and Na as well as north polar enhancements of Na.

Results reported here are from the analysis of a data set including six elongations of the planet Mercury between June 1986 and January 1988. Observations were made at the 1.5-m Cassegrain reflecting telescope at the Catalina Observatory, Mount Bigelow, Arizona (*11*). The spectrograph slit (~1 cm in height) was placed across the disk of Mercury in either a north to south orientation or in alignment parallel to Mercury's equator (*12*).

Two factors create conditions favorable to observing both K emission lines (*13*) from Mercury's atmosphere. Radial velocities up to 10 km/sec between Mercury and the sun shift the wavelength providing solar flux to excite the shorter, D2 line at 7665 Å. In addition, the large radial velocities between Earth and Mercury displace the emission lines in Mercury's atmosphere away from the telluric O_2 lines. Observing when both lines are visible provides two measurements of resonantly scattered light which can be independently converted into column abundances of the scattering constituent.

Potassium has a substantial advantage over Na for mapping of the atmosphere. While cross sections at line center in the two fine-structure components of K are relatively large (*14*), column abundances N, of K are relatively low (10^8 to 10^{10} K atoms/cm^2). The low intensity makes observations difficult, but still feasible with modern equipment. The typical optical thickness of the more easily observed sodium is such that the intensity changes more slowly with abundance.

For an optically thin atmosphere such as the K atmosphere at Mercury, the rate of emission (*15*) is $\mu 4\pi I = gN$ photons cm^{-2} sec^{-1}; where N is the vertical column abundance (atoms cm^{-2}), g is the photon-scattering coefficient (photons sec^{-1} atom^{-1}), and μ is the cosine of the angle made by the local zenith and the path from the planet's surface to the observer. The rate of emission from a 1-cm^2 column along the line of sight, $4\pi I$, is expressed in Rayleighs (10^6 quanta cm^{-2} sec^{-1}) after Hunten *et al.* (*16*). The quantity g varies with exciting frequency (*17*). Thus intensity is directly proportional to the line of sight abundance of K, along with the geometrical factors which are easily calculated. In this work, the brightness of Mercury's surface was used as an intensity standard (*18*).

Table 1 shows a log of observations and relevant parameters for each frame analyzed and presented here; the K column abundances are shown in Fig. 1. Slit orientation is north-south in all cases. An average viewing angle was calculated for the spatial element sampled. Horizontal sectors represent units of 20° longitude and are labeled. Because of smearing due to atmospheric turbulence (seeing) and to drift of the slit during exposure, spatial resolution falls short of the theoretical ideal (0.157 arc second per pixel) by a large factor (*19*). The illuminated longitude range visible from Earth typically varies from 60 to 110° because observations are made near greatest elongations from the sun. The longitude range beneath the slit is determined by geometric projection effects, guiding accuracy and atmospheric turbulence. Vertical divisions in Fig. 1 (and Table 1, labeled N, C, and S) represent three

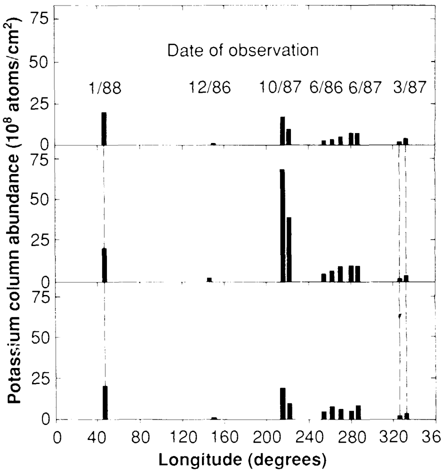

Fig. 1. Vertical bars represent potassium column abundances in units of 10^8 atoms/cm^2. Three latitudinal resolution sectors or bins are shown. The top rectangle shows abundances roughly corresponding to north polar and high northern latitudes; the central rectangle abundances from mid, low, and equatorial latitudes; the bottom sector abundances from south polar and high southern latitudes. The longitude on Mercury's surface beneath the atmospheric measurement is shown along the horizontal axis. The longitude should be interpreted as roughly locating the center of the beam, which can be seen from Fig. 2 to extend over many degrees. Dotted vertical lines connecting bars in January 1988 and March 1988 indicate global averages and should not be interpreted as observations showing no latitudinal variation. Caloris Basin is centered at about 200° longitude.

Department of Planetary Sciences, University of Arizona, Tucson, AZ 85721.

*Present address: NASA Ames Research Center, Moffett Field, CA 94035.

broad latitudinal sectors, roughly described as north polar, mid-latitudes and equatorial, and south polar zones. In some frames greater spatial resolution was obtained but for ease of plotting they were rebinned into three resolution elements. The histogram in each box represents the zenith column abundance found for that sector. Where only an average value was obtained for the observed area, the same value is shown in each latitudinal box with a dotted line connecting them to indicate that the values are not to be interpreted as representing uniform distribution. Figure 2 illustrates the relationship between the illuminated portion of Mercury, the beam size (spatial resolution element) and longitude for the observing period in October 1987.

The outstanding feature of Fig. 1 is at 220° longitude where the average column abundance is 2.7×10^9 K atoms/cm^2, a factor of ~5 greater than the typical value from all other data, $\sim 5.4 \times 10^8$ K atoms/cm^2. This longitude falls over Caloris Basin centered at ~200° longitude (Fig. 2). Because of atmospheric turbulence, the sampled atmosphere in these two frames is primarily that from above the Caloris Basin and slightly to the southwest. Although we have reported latitudinal asymmetries in neutral potassium before (*9, 10*), this is the first report associating such large enhancements with a specific surface feature. The high slit average (~4 greater than the mean of all the data) seen near 45° longitude may be associated with the badly fractured terrain antipodal to Caloris. Troughs viewed on the surface by Mariner 10 are interpreted as graben which formed during vertical ground motions induced by focused seismic waves from the Caloris impact (*20*).

The relatively large column abundances observed above the region near 220° longitude can be attributed to the increased diffusion of K from the crust and regolith in the Caloris Basin region. There, severe fracturing penetrates to depth and creates a physically conducive medium for transport of K out of rock assemblages into the network of micro-fractures and cracks where rapid regolith diffusion carries them to the surface-vacuum interface and they are liberated into the atmosphere (*21*).

Ionization is the most important loss process of Na and K from the atmosphere. Because of Mercury's highly eccentric orbit, the time required for solar ultraviolet radiation to ionize all but 1/*e* of the neutral population varies as shown in Table 1. Once the neutrals are ionized, electric fields generated by interaction of the inherent magnetic field with the solar wind, sweep a large fraction of them into the interplanetary medium where they are lost from the atmosphere (*22*). Some fraction impact the surface, are neutralized and are recycled into the atmosphere by evaporation or sputtering from the surface.

Except in limited regions near the terminator where radiation acceleration is directed parallel to the ground, potassium does not move far about the planet before it is ionized. Once a neutral Na or K atom is in the atmosphere it is controlled by its physical interactions with the solar ionizing flux and with the surface. A general discussion of gas-surface interactions on Mercury's surface can be found in Hunten *et al.* (*23*). When a Na or K atom leaves the surface on a ballistic trajectory with energy commensurate to a surface temperature of ~500 K the average trajectory distance is approximately

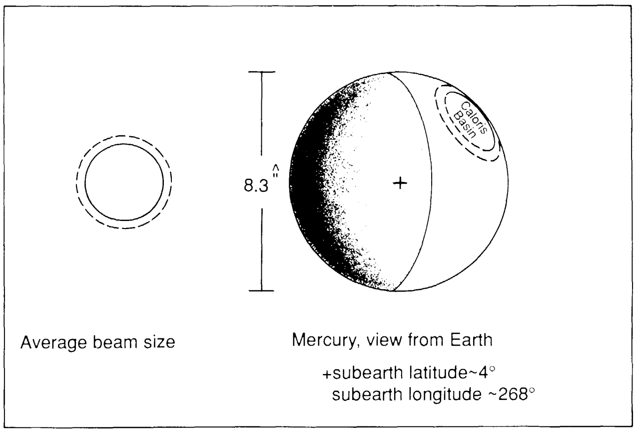

Fig. 2. The relative sizes of the sunlit portion of Mercury and the average resolution element (beam size) are shown. The diameter of Mercury (8.3 arc seconds) is shown for the day observations were made of the longitude range containing Caloris Basin.

Table 1. Observations of atmospheric potassium. Exposure times vary from 3 to 6 minutes. N, C, and S correspond to the latitude bins of Fig. 1. The phase angle is measured at the center of an illuminated body between the light source and the observer.

Line, frame number sector		Time UT	Phase angle (degrees)	Heliocentric distance (AU)	g (s^{-1})	Emission rate (kilo-rayleighs)	Cosine emergent angle
				19 June 1986			
D2, 58,	N	0253	88	0.416	81	26.7	0.88
	C					49.1	0.94
	S					49.2	0.89
D2, 59	N	0301	88	0.416	81	35.4	0.87
	C					70.7	0.94
	S					63.7	0.89
D2, 60	N	0312	88	0.416	81	53.4	0.91
	C					66.5	0.95
	S					63.7	0.92
				2 December 1986			
D1, 63	N	1334	68	0.365	61	14.3	0.78
	C					24.5	0.91
	S					13.0	0.80
				13 March 1987			
D1, 99	All	1315	118	0.433	40	16.9	0.86
D2, 101	All	1341	118	0.433	76	13.5	0.82
				8 June 1987			
D1, 76	N	2206	108	0.433	37	22.6	0.73
	C					48.3	0.85
	S					29.2	0.75
				9 June 1987			
D2, 93	N	0251	108	0.429	70	65.3	0.74
	C					78.3	0.87
	S					78.3	0.76
				14 October 1987			
D1, 291	N	2132	107	0.395	52	123	0.72
	C					426	0.90
	S					126	0.74
D2, 296	N	2222	107	0.395	100	116	0.72
	C					153	0.90
	S					104	0.75
				22 January 1988			
D2, 40	All	0110	32	0.331	129	322	0.84

the same as its scale height. An ensemble of neutral atoms will make only tens of hops before most are ionized (see Table 2 for relevant parameters). If the K atoms bounce in a random walk from a localized source region, the ensemble will not spread beyond ~180 km from the source region (*24*). Potassium, with its smaller scale height, shorter flight distance and shorter ionization time becomes the preferred species over sodium for mapping spatial variations.

The diameter of the inner Caloris Basin is roughly 1300 km. Concentric rings appear at greater distances outward from this main ring giving a maximum diameter of at least 1700 km to this impact feature. The basin interior is filled with extensively ridged and fractured plains. Well-fractured terrain extends outward beyond the Caloris Montes range for another 500 km or so. The impact that created Caloris Basin and associated ridges and fractures is dated by Strom and Neukum (*25*) and placed near the end of late heavy bombardment at Mercury, and following the period of core formation. Thus, it seems likely that the basin is underlain by deeply fractured material (*26*).

At the longitudes of the "hot poles" (*27*) sustained subsurface heating could increase the efficiency of alkali atoms diffusing to the surface. If the source flux is limited by grain boundary diffusion at depth (~10 km), the warmer subsurface materials at these longitudes will provide only a second order effect as atoms diffuse more rapidly through the cracks to the surface. If the source flux is limited by the physical properties of the crust and regolith through which atoms must traverse to make their way from the deeper source to the surface, then the higher subsurface temperatures associated with the "hot poles" could contribute to the increase in abundances observed at the longitudes near Caloris and the antipodal terrain. Of course we cannot rule out a stochastic process such as the serendipitous volatilization of a large impactor.

A source directly coupled to insolation (evaporation or photodesorption) would show maximum enhancements when the hot longitudes are near the subsolar point at perihelion. Although the observation near 45° longitude falls close to perihelion, the one near Caloris does not.

Recycling of ions to the cooler surface beneath the polar cusps of the magnetic field where they undergo neutralization and subsequent reintroduction into the neutral atmosphere has been suggested (*28, 30*) as a source of some observed enhancements. Ip (*29*) and Goldstein *et al.* (*22*) have estimated recycling efficiency to be about 50%, too small to explain the factor of ~5 seen at 220° and ~4 at 40°.

Table 2. Transport parameters for sodium and potassium at Mercury.

Parameter	Sodium	Potassium
Diameter Caloris Basin, 1300 km		
Hop time T (min)	~3	~2
Scale height at 500 K; H (km)	~49	~32
Hop distance d, (km)	~49	~32
Ionization time τ_i (hours)		
Perihelion	1.4	1.0
Aphelion	3.2	2.2
Distance traversed before ionization; D (km)	~350	~180

While this report was under review the work referenced in (*18*) was published (*30*). The most intense region in figure 1 of (*30*) (omitted from the summary of "emission patches" in their table 2) falls over Caloris Basin. The largest and brightest patch of figure 2 of (*30*) coincides with the antipodal terrain. This patch changed intensity over a period of one Earth day, implying that degassing would be variable. The maximum intensity areas of figure 3 of (*30*) are over regions not imaged by Mariner 10, and those of figure 4 of (*30*) have not been correlated with any major surface feature.

The increased diffusion of alkali atoms from the crust and regolith from regions of deep fracture is probable as a cause of the enhancements of K emission presented here. Significantly larger abundances found in this data set occurred when Caloris Basin or its antipodal point were in the field of view. This is good evidence that the increased fracturing associated with Caloris Basin formation provides localized enhancements to the global source mechanism, diffusion of atoms outwards from subsurface materials.

REFERENCES AND NOTES

1. The atmosphere at Mercury is really a vacuum by terrestrial standards (~10^{-12} bar). The only collisions of atoms are likely to be with the surface, so atoms can be regarded as moving in ballistic orbits intersecting the surface on most occasions. A comprehensive summary is given by Hunten *et al.* (*23*).
2. A. E. Potter and T. H. Morgan, *Science* **229**, 651 (1985).
3. ———, *Icarus* **67**, 336 (1986).
4. M. A. McGrath, R. E. Johnson, L. J. Lanzerotti, *Nature* **323**, 694 (1986).
5. T. H. Morgan, H. A. Zook, A. E. Potter, *Icarus* **74**, 156 (1988).
6. A. L. Sprague, *Lunar and Planetary Science XX* (Lunar and Planetary Institute, Houston, 1989), pp. 1040–1041.
7. Diffusion from surface grains as a source of Na and K in Mercury's atmosphere was suggested in A. F. Cheng *et al.*, *Icarus* **71**, 430 (1987). However, the mechanism is distinct from the one presented here.
8. A. E. Potter and T. H. Morgan, *ibid.*, p. 472.
9. A. L. Tyler, R. W. Kozlowski, N. M. Schneider, *Bull. Am. Astron. Soc.* **19**, 862 (1987).
10. A. L. Tyler, N. M. Schneider, W. K. Wells, D. M. Hunten, R. W. Kozlowski, *ibid.* **18**, 781 (1986).
11. The instrumentation gives a dispersion of 0.029 Å per pixel in the CCD image. A blocking filter of ~100 Å full width half maximum was used to prevent transmission of light from other wavelengths at higher or lower orders.
12. The entire planet along with considerable sky at both top and bottom was subtended by the spectrograph slit. The three-dimensional spectral images (spatial, along the slit; spectra, in dispersion; intensity, counts, or data numbers) were stored in 512 by 512 pixel Texas Instrument CCD images. These images were then corrected for dark current and varying sensitivity within the electronics of the CCD, imperfections in the optical path of the telescope and, spectrograph, curvature and nonlinear dispersion with wavelength, and, if required, for daylight telluric scattering and absorption.
13. Observed is the ground-state excitation of neutral K in the fine structure components at 7698.98 Å ($^2P_{1/2} - {}^2S_{1/2}$) and 7664.9 Å ($^2P_{3/2} - {}^2S_{1/2}$).
14. The cross sections at line center are $\alpha_{o1} = 8.6 \times 10^{-12}$ and $\alpha_{o2} = 1.7 \times 10^{-11}$ cm^2 for potassium D2 and D1 lines, respectively.
15. J. W. Chamberlain and D. M. Hunten, *Theory of Planetary Atmospheres* (Academic Press, New York, ed. 2, 1987).
16. D. M. Hunten, F. E. Roach, J. W. Chamberlain, *J. Atmos. Terr. Physics* **8**, 345 (1956).
17. The D2 line is stronger by a factor of 2 over D1 due to the greater oscillator strength. In addition the modulating factors of the Mercury-Sun radial velocity which shifts line center in Mercury's reference frame, and the $1/r^2$ change in solar flux as Mercury moves in its eccentric orbit, cause the scattering probability to vary dramatically from the minimum D1 value of ~10 scatters per second to the maximum D2 value of ~170 scatters per second.
18. Correction for Earth atmospheric extinction can be made by calibrating the flux in the emission lines to the light scattered from Mercury's surface in the same exposure. Reflectance factors are calculated using Hapke scattering theory code provided by Paul Helfenstein.
19. A one-dimensional seeing deconvolution algorithm is used to partially correct for the smearing of the image. It is not possible to recover all spatial information. In fact, it was determined that at most, four spatial elements could be extracted reasonably from these observations and only in the case where the maximum extent of the sunlit hemisphere was subtended in a direction oriented parallel to the north-south axis.
20. P. H. Shultz and D. E. Gault, *Moon* **12**, 159 (1975).
21. A. L. Sprague, *Icarus* **84**, 93 (1990).
22. B. E. Goldstein, S. T. Suess, R. J. Walker, *J. Geophys. Res.*, **86**, 5485 (1981).
23. D. M. Hunten, T. H. Morgan, D. M. Shemansky, in *Mercury*, F. Vilas, C. Chapman, M. S. Matthews, Eds. (Univ. of Arizona Press, Tucson, AZ, 1988), pp. 561–611.
24. The time of flight T, sustained by an atom in a ballistic trajectory is: $T = \sqrt{2\pi H/g}$ where H is the barometric scale height and g the acceleration due to gravity. The migration distance D can be calculated for a random walk of atoms from the point of origin by $D = H\sqrt{\tau_i/T}$. Symbols are defined in Table 2.
25. R. E. Strom and G. Neukum, in *Mercury*, F. Vilas, C. Chapman, M. S. Matthews, Eds. (Univ. of Arizona Press, Tucson, AZ, 1988), pp. 336–373.
26. R. E. Strom, in *Geology of the Terrestrial Planets*, M. H. Carr, Ed. (NASA SP-469, 1984), pp. 13–56.
27. Because of the 3:2 spin-orbit coupling of Mercury, the total heating of the surface varies greatly. The effects of insolation are permanently locked into the surface. Two longitudes, 0 and 180° are always at the subsolar point during perihelion. These have been termed the "hot poles" by S. L. Soter and J. Ulrichs [*Nature* **214** 1315 (1967)].
28. R. M. Killen and T. H. Morgan, *Bull. Am. Astron. Soc.* **21**, 975 (1989).
29. W. F. Ip, *Icarus* **71**, 441 (1987).
30. A. E. Potter and T. H. Morgan, *Science* **248**, 835 (1990).

31. Special thanks are given to M. Leake for interesting discussions concerning Caloris Basin. We are also grateful to: E. Karkoschka, N. Schneider, and K. Wells for assistance at the telescope and with data analysis; W. Smyth for his help with topics regarding radiation acceleration; K. Linker and D. Yoder for computational assistance; B. Rizk for mapping software; U. Fink for use of his CCD data acquisition system; the UAO telescope allocation committee and scheduling teams for adequate telescope time including the dates required to make these observations. The research was funded by NASA grants NGT 5005065 and NAG2 143 and a Whitaker Foundation grant of the Research Corporation.

5 December 1989; accepted 26 June 1990

Hole Density Dependence of the Critical Temperature and Coupling Constant in the Cuprate Superconductors

M.-H. WHANGBO AND C. C. TORARDI

A bond valence sum (BVS) analysis was performed for the p-type cuprate superconductors. The superconducting critical temperature T_c versus in-plane Cu-O BVS correlation for copper is grouped into classes and subclasses. Only within a class or subclass for which the nonelectronic effect is constant does the variation of the in-plane Cu-O BVS reflect the corresponding change in the hole density n_H of the CuO_2 layers. This study strongly suggests that the T_c for every class or subclass of the superconductors is an inverted parabolic function of n_H, and so is the coupling constant λ for Cooper pair formation.

IN UNDERSTANDING THE SUPERCONductivity of the cuprate superconductors it is vital to know what structural or electronic factors govern the magnitudes of their superconducting critical temperatures T_c. The T_c values of the p-type cuprate superconductors have been correlated with a number of parameters, which include the hole densities (n_H) per CuO_2 unit in the CuO_2 layers (*1–9*), the Madelung potentials (*10, 11*), the electronegativities (*12–15*), the in-plane Cu-O bond lengths (*16, 17*), the electronic densities of states at the Fermi level (*18*), the bond valence sums (BVSs) (*19–23*), and the hole density to effective mass ratios (*24*). Oxidation of the CuO_2 layers (that is, hole doping) removes electrons from the x^2-y^2 bands which have antibonding character in the in-plane Cu-O bonds (*25, 26*). As n_H increases, therefore, the in-plane Cu-O bond length ($r_{Cu\text{-}O}$) is shortened. In addition to this electronic factor, the in-plane $r_{Cu\text{-}O}$ is also controlled by the nonelectronic factor (*16, 17*) (for example, steric strain) associated with the cations located at the 9-coordinate sites adjacent to the CuO_2 layers (see Fig. 1, top). With the increasing size of the 9-coordinate site cations, the in-plane Cu-O bond is lengthened to reduce the extent of the resulting steric strain. The T_c versus in-plane $r_{Cu\text{-}O}$ plot of the p-type cuprate superconductors is grouped into three classes distinguished by the size of the 9-coordinate site cations (that is, La-, Sr-, and Ba-classes) (*16, 17*) because of the combined electronic and nonelectronic effects. The Sr- and Ba-classes contain subclasses which are further distinguished by a secondary nonelectronic factor associated with the number of CuO_2 layers per unit cell or the cation substitution in the rock salt layers. Every class or subclass of the T_c versus in-plane $r_{Cu\text{-}O}$ plot shows a maximum, so that every class or subclass of the p-type cuprate superconductors possesses an optimum hole density (n_{opt}) for which the T_c is maximum ($T_{c,max}$) (*16, 17*).

By definition, the bond valence of an in-plane Cu-O bond should increase with the shortening of its length (*27, 28*). Since the in-plane $r_{Cu\text{-}O}$ decreases with increasing n_H, the BVS of an in-plane Cu atom obtained only from its in-plane Cu-O bonds (hereafter referred to as the in-plane BVS) is expected to increase with increasing n_H. Therefore, a T_c versus in-plane BVS plot should have a maximum as in the corresponding T_c versus in-plane $r_{Cu\text{-}O}$ plot. The steric factor associated with the 9-coordination site cation affects the in-plane $r_{Cu\text{-}O}$ value and hence the corresponding in-plane BVS value. Therefore, the T_c versus in-plane BVS plot for the p-type cuprate superconductors should separate into La-, Sr-, and Ba-classes and their subclasses as in the case of the T_c versus in-plane $r_{Cu\text{-}O}$ plot. This expectation is borne out as will be shown below. The present work strongly suggests that the T_c for each class or subclass is an inverted parabolic function of the in-plane BVS or the hole density n_H. This relationship leads to an important constraint that the coupling constant λ for Cooper pair formation is an inverted parabolic function of n_H.

The bond valence s_i of a bond i is defined

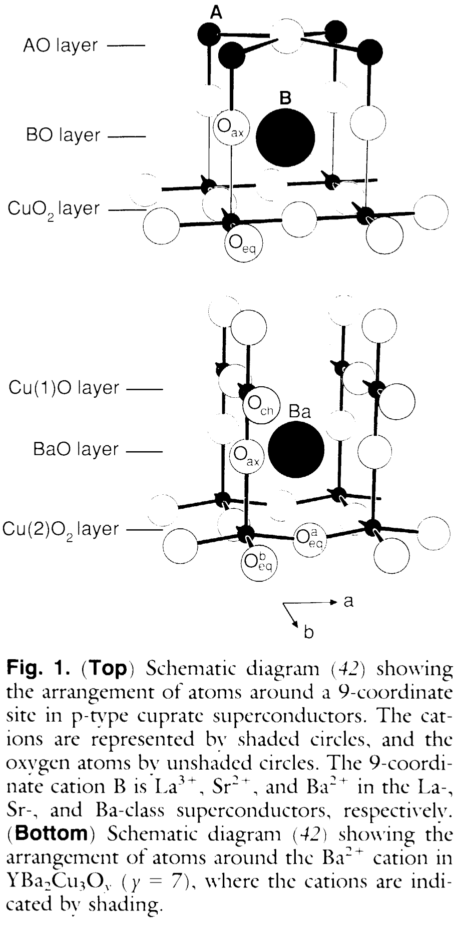

Fig. 1. (**Top**) Schematic diagram (*42*) showing the arrangement of atoms around a 9-coordinate site in p-type cuprate superconductors. The cations are represented by shaded circles, and the oxygen atoms by unshaded circles. The 9-coordinate cation B is La^{3+}, Sr^{2+}, and Ba^{2+} in the La-, Sr-, and Ba-class superconductors, respectively. (**Bottom**) Schematic diagram (*42*) showing the arrangement of atoms around the Ba^{2+} cation in $YBa_2Cu_3O_y$ (y = 7), where the cations are indicated by shading.

Table 1. Calculated α, V_{opt}, and RMSE (root-mean-square error) values from the least-squares fitting of the La-, Sr- and Ba-classes and their subclasses with the equation* $\Delta T_c = -\alpha(\Delta V)^2$.

Compounds	$\alpha \times 10^{-4}$	V_{opt}	RMSE†
Ba-class	2.72 ± 0.18	2.05	7.1
Sr-class	3.20 ± 0.53	2.15	11.0
La-class[a]	2.46 ± 0.53	2.27	4.9
$(Tl_{2-x}Cd_x)Ba_2CuO_6$ subclass[b]	6.09 ± 1.01	2.04	7.7
$Bi_2Sr_2(Ca_{1-x}Y_x)Cu_2O_8$ subclass[c]	5.78 ± 0.70	2.12	4.8
$(Tl_{0.5}Bi_{0.5})Sr_2(Ca_{1-x}Y_x)Cu_2O_7$ subclass[d]	4.85 ± 1.04	2.18	10.0

*BVS calculated using the in-plane $r_{Cu\text{-}O}$ values from: [a]Tarascon *et al.* (*30*) for $La_{2-x}Sr_xCuO_4$; [b]Parise *et al.* (*41*); [c]Groen and de Leeuw (*32*); [d]Huang *et al.* (*33*). †Standard deviations of the observed T_c values from the quadratic fits.

M.-H. Whangbo, Department of Chemistry, North Carolina State University, Raleigh, NC 27695-8204.
C. C. Torardi, Central Research and Development Department, E. I. du Pont de Nemours and Company, Experimental Station, Wilmington, DE 19880-0356.